

Numerical Evaluation of Different Pulverized Coal and Solid Recovered Fuel Co-firing Modes Inside a Large-scale Cement Calciner

Hrvoje Mikulčić^{*,a}, Eberhard von Berg^b, Milan Vujanović^a, Xuebin Wang^c,
Houzhang Tan^c, Neven Duić^a

^a Faculty of Mechanical Engineering and Naval Architecture
University of Zagreb, Zagreb, Croatia

e-mail: hrvoje.mikulcic@fsb.hr, milan.vujanovic@fsb.hr, neven.duic@fsb.hr

^b AVL List GmbH, Hans List Platz 1, Graz, Austria
e-mail: eberhard.von.berg@avl.com

^c MOE Key Laboratory of Thermo-Fluid Science and Engineering, Xi'an Jiaotong University,
Xi'an 710049, China

e-mail: wxb005@xjtu.edu.cn, tanhz@mail.xjtu.edu.cn

Abstract

Partial substitution of coal by alternative solid fuels, such as waste-derived fuels and biomass, is recognized as an advantageous method for greenhouse gas mitigation. However, due to different fuel properties than that of coal, alternative fuels have a direct impact on the performance of existing pulverized coal fired furnaces. Numerical simulations currently represent a useful approach for studying and controlling the co-firing process. Early comprehensive information, parametric studies and initial conclusions that can be gained from numerical simulations are very important in handling modern combustion units. In this study modelling approach for the combustion of pulverized coal, biomass, plastic, and solid recovered fuel is presented. The purpose of the present study is to evaluate six different pulverized coal and solid recovered fuel co-firing modes inside a cement calciner. The thermal share of the solid recovered fuel in these six simulations varied from 0 % to 100 %. The results obtained, which include the temperature and species concentrations, provide useful conclusions regarding the maximal allowed coal substitution rate for stable cement calciner operation.

* Corresponding author. Tel.: +385 1 6168 494; fax: +385 1 6156 940.
E-mail address: hrvoje.mikulcic@fsb.hr (H. Mikulčić).

Keywords: Co-firing; Cement calciner; Pulverized coal; Solid recovered fuel; Numerical evaluation

1. Introduction

Coal continues to be one of the major energy sources within all industrial sectors worldwide despite its high CO₂ emission potential [1]-[2]. Partial substitution of coal with alternative solid fuels, such as waste-derived fuels and biomass, in existing combustion units is recognized as one of the most convenient and advantageous methods for greenhouse gas (GHG) mitigation [3]. Unlike fossil fuels, biomass and biomass-rich waste-derived fuels are considered renewable and CO₂-neutral because biomass, including biomass residue, if deposited and not used, decays and produces methane and other decomposition products that greatly exceed the potency of CO₂ as a greenhouse gas [4]. The other benefit from using alternative solid fuels in existing pulverized coal fired furnaces is the preservation of space in existing landfills [5]. As waste disposal at landfills is the last option in the waste management strategy, energy recovery of waste-derived fuels is being increasingly promoted [6]. Waste-derived fuels are produced from municipal solid waste (MSW) using a mechanical biological treatment (MBT) process. This fuel is prepared from non-hazardous waste materials intended for firing in industrial furnaces [7]. Over the past few years, the name of the waste-derived fuels has changed. Although refuse-derived fuel (RDF) is the most common name used for such a fuel, new standards define this fuel as solid recovered fuel (SRF). RDF had only two classes depending only on the calorific value, moisture and ash content, in contrast to 125 SRF classes. These SRF classes are based on three properties where each of the properties has five classes for the net calorific value, the chlorine content, and the mercury content [8]. Although substitution of fossil fuels by alternative solid fuels is recognized as a method for GHG mitigation, alternative solid fuels, due to their different fuel properties, have been reported to have a direct impact on the performance of existing pulverized coal fired furnaces [9]. Therefore, over the few last years, many research investigations have been carried out in this field [10].

Numerical simulations currently represent a useful approach for studying different furnace geometries and the effects of different fuels and are much faster and cheaper than an experimental investigation [11]. The computational cost of such numerical simulations is very dependent on the level of accuracy of the adopted modelling approach. Accurate modelling of combustion units co-firing alternative fuels is essential to reveal potential problems that may occur during the first experimental trials [12].

In the reported literature, there are several studies that have investigated the direct co-combustion of alternative fuels in utility boilers and small-scale furnaces. Bhuiyan and Naser [13] numerically investigated the co-firing of biomass with coal in an oxy-fuel condition in a small-scale furnace. This study showed that for the analysed furnace, an increase in the biomass fuel share was responsible for increasing the flame volume and decreasing the peak temperature. The study also showed that special care must be taken to optimize the biomass share and recycled ratio to achieve stable radiative, convective heat transfer and burnout performance. Dong et al. [14] investigated the co-firing of coal and the product gas from biomass gasification in a 600 MWe tangential pulverized coal fired boiler. This study showed that a decrease in NO_x emission of approximately 50–70% can be achieved when the product gas was injected through the lowest layer burner. Holtmeyer et al. [15] studied the effect of biomass particle size on the flame structure and NO formation. The study showed that co-firing flames had longer flame envelopes compared with coal-only flames due to the increased volatile matter within the biomass. Furthermore, the study showed that the use of larger biomass particles resulted in increased NO formation. Gubba et al. [16] investigated the co-firing of straw and coal in a 300 MWe pulverized fuel fired boiler. Their prediction of the temperature profile, NO_x formation, and char burnout was in good agreement with the reported measurements. Karampinis et al. [17] analysed the co-combustion of lignite and cardoon in a tangentially fired furnace. The study showed that a decrease in NO_x emissions of up to 10% can be achieved when cardoon is co-combusted with coal. This is mostly due to the lower nitrogen content of the biomass compared with coal. Agraniotis et al. [18] evaluated different coal and SRF co-combustion modes in a 600 MWe boiler. This study showed that with regard to the evaluation of different co-combustion scenarios in utility boilers, CFD modelling is more advantageous than experimental studies, which can be more time-consuming and costly.

However, aside from the studies analysing the co-firing concept in utility boilers, to the knowledge of the authors, there have been only a few studies that have analysed the co-firing of alternative fuels in cement furnaces. Ariyaratne et al. [19] analysed meat and bone meal (MBM) combustion in a cement rotary kiln with different fuel feeding positions. This study emphasised the importance of fine fuel grinding. An observation was made that MBM particles needed more time to fully combust than coal particles. This was due to the high moisture and ash content, slower devolatilisation and greater air demand of the MBM. Mikulčić et al. [20] studied different biomass co-combustion shares in a cement calciner. This study showed that when combusting biomass in existing pulverized fuel burners and due to the different kinetics, special

attention needs to be given to the complete particle burnout to avoid undesirable instabilities in the raw material preheating system.

To date, to the authors' knowledge, there have been no numerical studies that have investigated the thermal and process implications of the SRF co-firing process inside a cement calciner. Therefore, the purpose of the present study is to fill this knowledge gap. With regard to the regions with interesting flow and mixing phenomena and the optimisation of key physical and chemical processes inside cement calciners, the present approach, which uses separately previously validated models for the calcination process and the combustion of different pulverized solid fuels [21], improves the available CFD simulation methodology. Due to the high reliability of the separately validated models, appropriate accuracy, which is needed for the investigation of the details and for the optimisation of key physical and chemical processes within cement calciners, can be achieved. The present study evaluates different pulverized coal and SRF co-firing modes inside a cement calciner and the effect of the mode on the calciner's operating conditions taking into account the major physical and chemical processes of coal and the SRF combustion process. Different co-firing modes have a different effect on the calciner's operating conditions, so this study also brings added value to the investigations related to SRF as an alternative fuel inside a cement calciner. To evaluate different co-firing modes, six different co-firing modes were simulated to investigate the influence on the flame shape and pollutant formation. The thermal share of SRF in these six simulations varied from 0 % to 100 %. The results obtained from this study can be used to better understand the co-firing process inside the calculated calciner. Finally, it should be stated that the numerical models that were used for the analyses of different SRF co-firing processes only analysed the pollutants, such as CO₂, CO, and CH₄. The analysis of the formation of pollutants, such as NO, Cl and Hg, will be performed in future work.

2. Numerical method

When modelling the solid fuel combustion process, one has to account for the multiphase nature of this process, which involves both the solid and the gas phases, their interaction and the production and transport of solid particles [22]-[23]. The Eulerian-Lagrangian modelling approach, which is the most widely used approach for the numerical computation of the multiphase flow phenomena [24], is used in the presented work. Additionally, in the present study and in most studies found in the literature when pulverized fuel (PF) flames are analysed, the simplification for the PF particles is that the temperature is uniform throughout the particle (isothermal particles) at any given time [25]. Therefore, the description of the particle

conversion processes can be significantly simplified. The overall approach used for the numerical computation of the multi-phase flow and a series of particle conversion processes have been well documented in our previous studies.

Table 1 shows an overview of previous studies where the modelling approach for the coupling of the gas and the solid phase, the thermal decomposition of limestone, the combustion of each solid fuel, and a comparison between experimental data and the numerical predictions is given. However, to ensure the integrity of the present study, the modelling approach for the combustion of each solid fuel is given in detail.

2.1. Gaseous phase

The gaseous phase is solved in the Eulerian frame of reference using the conservation laws for mass, momentum and energy. The differential form of the mass conservation equation is:

$$\frac{\partial \rho}{\partial t} + \frac{\partial(\rho v_j)}{\partial x_j} = S_c. \quad (1)$$

The differential form of the momentum conservation equation is:

$$\frac{\partial(\rho v_i)}{\partial t} + \frac{\partial(\rho v_j v_i)}{\partial x_j} = -\frac{\partial p}{\partial x_j} + \frac{\partial}{\partial x_j} \left[\mu \left(\frac{\partial v_j}{\partial x_i} + \frac{\partial v_i}{\partial x_j} - \frac{2}{3} \frac{\partial v_k}{\partial x_k} \delta_{ij} \right) \right] + \rho g_i + S_M, \quad (2)$$

with i , j , and k denoting coordinate indices and where the terms in the square brackets on the right side represent the stress tensor:

$$\tau_{ij} = \mu \left(\frac{\partial v_j}{\partial x_i} + \frac{\partial v_i}{\partial x_j} - \frac{2}{3} \frac{\partial v_k}{\partial x_k} \delta_{ij} \right). \quad (3)$$

The differential form of the energy conservation equation is:

$$\frac{\partial(\rho E)}{\partial t} + \frac{\partial(\rho v_j E)}{\partial x_j} = -p \frac{\partial v_j}{\partial x_j} + \frac{\partial}{\partial x_j} \left(\lambda \frac{\partial T}{\partial x_j} \right) + \tau_{ij} \frac{\partial v_i}{\partial x_j} + S_E. \quad (4)$$

In addition to the conservation equations for n species, the following species transport equation is solved:

$$\frac{\partial}{\partial t} (\rho Y_l) + \frac{\partial}{\partial x_j} (\rho v_j Y_l) = \frac{\partial}{\partial x_j} \left(\Gamma \frac{\partial Y_l}{\partial x_j} \right) + S_{Y_l}, \quad l = 1, \dots, n. \quad (5)$$

The source terms S on the right side of each conservation equation and in the species transport equation are used to couple the continuous and solid phase, e.g., the coupling of the Eulerian and the Lagrangian frame of reference due to the heterogeneous reactions. Additionally, the source term in the species transport equation is due to the production or consumption of species mass fraction by homogeneous reactions in the continuous phase. The conservation equations are solved using a finite volume method providing the temporal evolution and spatial distribution of velocities, temperatures and concentrations. Gas phase chemistry can be defined via input files containing the desired gas phase reactions and is treated via a separate chemistry solver between the time steps of the gas phase solver [29].

2.2. Solid phase

The motion and transport of the solid particles are described using the Lagrangian frame of reference. The momentum differential equation is used to calculate the particle trajectories:

$$m_p \frac{du_{ip}}{dt} = F_{idr} + F_{ig}. \quad (6)$$

Further energy and mass conservation equations are solved for each particle as described in the following sections taking into account all of the necessary thermo-chemical reactions of the solid fuel particles. The thermo-chemical reactions occur inside a particle as well as between particle components and continuous phase species. The described models and the thermo-physical property data of the described fuels were integrated into the commercial CFD code AVL FIRE[®] using its user-defined functions capability [29].

2.3. Calcination process

Raw materials used in the production of cement are mainly composed of limestone. In the cement calciner, limestone thermally decomposes to lime and carbon dioxide according to the following endothermic reaction:



This reaction is extensively used in the cement industry because lime is a key ingredient in the final cement product. Approximately 60 % of the thermal energy used during the cement manufacturing is used for the calcination process. Because the calcination process has a direct influence on the overall energy efficiency of the cement production, the mixing phenomena

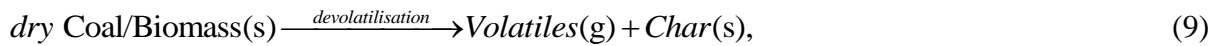
and heat exchange between the fuel and the limestone particles are of particular importance, as the calcination process is predominately a temperature-driven process [30].

A previously developed model was used in this study to correctly describe the calcination reaction inside the cement cyclone [28].

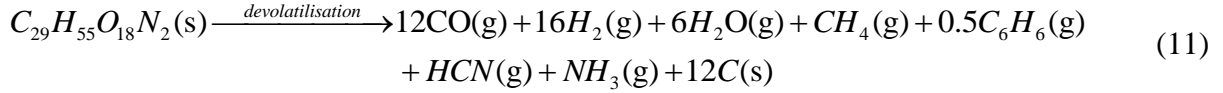
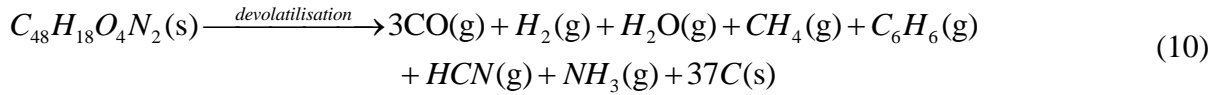
2.4. Coal/biomass combustion model

When pulverized coal and biomass particles travel through gas and interact with the gas in a furnace, they are rapidly heated up and undergo a series of conversion processes. Free moisture in the PF particles is evaporated quickly, followed by pyrolysis or devolatilisation in which pyrolysis gases or volatiles are released from the fuel particles. The volatiles are burned out in the gas phase. Once the pyrolysis is nearly complete, char oxidation dominates the heat release from the particle. During these processes, the particle temperature is constantly updated [31].

The pulverized coal/biomass combustion used in this study includes four steps: drying, devolatilisation, char burning, and combustion of volatiles. The four-step process for the combustion of the biomass and the coal particles has been reported in several recent studies [32]-[33]. The coal/biomass particle first undergoes the drying process, after which the devolatilisation starts.



After the drying process, the particle further heats up, and with an increase in the temperature, the devolatilisation process starts. During the devolatilisation, an important loss of weight occurs due to the release of volatile matter. The quantity and composition of the volatiles depend on the coal and biomass ingredients and the particle size and temperature. To elaborate more in detail the difference in the composition of the coal and the biomass particle, their dry-ash-free composition is given in Eqs. 10 and 11. The composition of coal (Eq. 10) and biomass (Eq. 11) and the volatile matter released during the devolatilisation are estimated from ultimate and proximate analysis of these two fuels. The ultimate and proximate analysis of coal and biomass used for the numerical modelling in this study is given in [34]-[35]. From Eqs. 10 and 11, it can be seen that depending on the type of the particle, there will be more or less char left in the particle after the devolatilisation, and there will be different amounts of volatile matter released during the devolatilisation.



After the devolatilisation, only char and ash are left in the solid particle. Parallel to the devolatilisation and depending on the particle size and temperature, char oxidizes to CO or CO₂, and subsequently, only ash remains. Then, the ash particle is considered inert, as only residual ash heating occurs.

The basic steps of drying, devolatilisation as well as combustion of volatiles and char oxidation occur for both fuels, coal and biomass. Main differences are in the composition of volatiles released and in the structural properties of the remaining char, i.e., porosity, tortuosity and size. The first issue is treated by different composition (see Eqs. 10 and 11), estimated from ultimate and proximate analysis of the fuels. The second issue is presently not treated due to lack of data, but is a topic for further work. For basic trends the presented approach is assumed to be sufficient, however for detailed analysis more detailed volatile composition as well as experimental data about structural properties of the fuels are needed.

2.4.1. Moisture evaporation

The model for the moisture evaporation considers two types of evaporation cases. The first case is the evaporation of water vapour due to the difference in water vapour concentration at the particle surface and in the gas, and the second case is the boiling process. The boiling process starts when the particle reaches the water boiling temperature, i.e., 100°C. It is assumed that during the boiling process, the particle temperature remains the same until all of the capillary-bounded water evaporates [36].

The mass flux of the water vapour is determined from the difference in the water vapour concentration at the particle surface and in the gas and is determined from:

$$\dot{m}_p = \frac{d_p^2 \pi}{10^3} M_{H_2O} k_w (C_p - C_g). \quad (12)$$

For the water vapour concentration at the particle surface, it is assumed that the water vapour partial pressure at the particle surface is equal to the water saturation pressure, p_{sat} , at a particle temperature T_p :

$$C_p = \frac{P_{sat}}{RT_p}, \quad (13)$$

and the water vapour concentration in the gas is given by the following equation:

$$C_g = X_{H_2O} \frac{P}{RT}. \quad (14)$$

The Sherwood number correlation by Ranz and Marshall [37] is used to calculate the mass transfer coefficient k_w :

$$Sh = \frac{k_w d_p}{D_w} = 2.0 + 0.6 Re_p^{1/2} Sc^{1/3}. \quad (15)$$

The Schmidt number is calculated according to the following equation:

$$Sc = \frac{\mu}{\rho D_w}. \quad (16)$$

The enthalpy balance of the drying particle at temperatures less than the water boiling temperature is calculated from the following expression:

$$m_p c_p \frac{dT_p}{dt} = \alpha A_p (T_g - T_p) + \varepsilon_p \sigma A_p (T_g^4 - T_p^4) + \dot{m}_p h_{latent}, \quad (17)$$

and, subsequently, during the boiling process and while the temperature is constant, the mass transfer is calculated according to:

$$\dot{m}_p = - \frac{\alpha A_p (T_g - T_p) + \varepsilon_p \sigma A_p (T_g^4 - T_p^4)}{h_{latent}}. \quad (18)$$

During the drying process, the water vapour mass flux becomes a source of water vapour in the water vapour species transport equation, and the water vapour mass flux multiplied by the latent heat becomes a source in the energy equation.

When the particle reaches the water boiling temperature, i.e., 100°C, the boiling process starts, which means that during the entire boiling process, the particle temperature remains the same until all of the capillary-bounded water is evaporated [36].

2.4.2. Devolatilisation and char combustion

After the drying process, the dry coal/biomass particles heat up further, and with an increase in the temperature, the devolatilisation process starts. The volatile matter is released from the particle, and char is produced. Instantly, as char is produced, oxidation begins, which means that the devolatilisation and char oxidation occur in parallel.

Numerically, the dry particle is composed of three parts: coal/biomass, char, and ash. The mass balance of the dry particle is expressed by the following equation:

$$m_p = m_{coal/biomass} + m_C + m_{ash}. \quad (19)$$

As explained previously, coal/biomass particles undergo devolatilisation, and the volatile matter is released and char is produced. Numerically, the change in the coal/biomass particle mass can be expressed as:

$$\dot{m}_{coal/biomass} = -\dot{m}_{C+} - \sum_{l=1}^n \dot{m}_{Y_l} / n_p, \quad (20)$$

where the first term on the right-hand side of the equation is the char production and the second term on the right-hand side is the sum of the production rates of all volatile species per particle.

The char mass changes due to char production during devolatilisation and due to char consumption during the char oxidation. This is calculated as:

$$\dot{m}_C = \dot{m}_{C+} + \dot{m}_{C-}. \quad (21)$$

The ash is assumed to be inert, and its mass does not change:

$$\dot{m}_{ash} = 0. \quad (22)$$

The overall particle mass changes due to the mass lost during the devolatilisation and the char oxidation:

$$\dot{m}_p = -\sum_{l=1}^n \dot{m}_{Y_l} / n_p + \dot{m}_{C-}. \quad (23)$$

The change in the mass fraction of the coal/biomass in the overall particle mass equals the devolatilisation reaction rate:

$$\frac{d}{dt} \left(\frac{m_{coal/biomass}}{m_p} \right) = -k_d. \quad (24)$$

After the term in brackets on the left-hand side of Eq. 24 is derived, the following expression is obtained:

$$\dot{m}_{coal/biomass} = -k_d m_p + \left(\frac{m_{coal/biomass}}{m_p} \right) \dot{m}_p, \quad (25)$$

and here, the change in coal/biomass mass is dependent on the devolatilisation reaction rate and is corrected according to the overall mass loss of the particle.

For the devolatilisation rate, k_d , a unified single rate expression is used, which means that the devolatilisation rate has a first-order dependency on the amount of coal/biomass mass fraction remaining in the particle (Eq. 26), and this relationship holds for all volatiles.

$$k_d = -k_1 y_{coal/biomass} \quad (26)$$

Here, for the kinetic rate k_I , an Arrhenius-type expression that includes a pre-exponential factor $k_{0,I}$ and an activation energy E_{aI} is used:

$$k_I = k_{0,I} \exp(-E_{aI} / RT_p) \quad (27)$$

The values of the devolatilisation kinetic constants, e.g., the pre-exponential factor and the activation energy for different coals and biomass, are obtained from the literature depending on which coal or biomass is modelled [34]-[35].

As the change in coal/biomass mass during the devolatilisation is now known (Eq. 25), the corresponding increase in the char mass and the mass of each volatile species depends on the stoichiometry of the devolatilisation and can be written in the following forms:

$$\dot{m}_{C+} = -|v_C| \left(\frac{M_C}{M_{coal/biomass}} \right) \dot{m}_{coal/biomass}, \quad (28)$$

$$\dot{m}_{Y_n} = -|v_{Y_i}| \left(\frac{M_{Y_i}}{M_{coal/biomass}} \right) \dot{m}_{coal/biomass} n_p. \quad (29)$$

As soon as some char is produced, char is oxidized to form CO and CO₂ taking into account the mechanism factor f_m :



The mechanism factor f_m depends on the char particle size and temperature and ranges between 1 and 2. This factor determines the shift from CO₂ to CO production with an increasing temperature and decreasing particle diameter, as shown in Eq. 30, and is calculated using the following expressions [38]:

$$f_m = \frac{2f_{CO} + 2}{f_{CO} + 2}; \quad d_p < 50 \mu m, \quad (31)$$

$$f_m = \frac{2f_{CO} + 2}{f_{CO} + 2} - \frac{f_{CO}(d_p - 50)}{(f_{CO} + 2) \cdot 950}; \quad 50 \mu m < d_p < 1000 \mu m. \quad (32)$$

The following expression is used to define f_{CO} :

$$f_{CO} = 2500 \cdot \exp(-6240 / T). \quad (33)$$

The decrease in the char mass fraction in the overall particle mass equals the char oxidation reaction rate:

$$\frac{d}{dt} \left(\frac{m_{C-}}{m_p} \right) = -k_{ox}. \quad (34)$$

After the term in brackets on the left-hand side of Eq. 34 is derived, the following expression is obtained:

$$\dot{m}_{C-} = -k_{ox} m_p + \left(\frac{m_C}{m_p} \right) \dot{m}_p. \quad (35)$$

Here, the decrease in the char mass in the overall particle mass is dependent on the char oxidation reaction rate and, again, is corrected for overall mass loss.

In this study, the overall char oxidation reaction rate is modelled according to the kinetics/diffusion limited reaction model of Baum and Street [36]. The model assumes that the reaction rate of char oxidation is limited either by oxygen's diffusion into the particle's mass, which is expressed by the value of k_2^{ph} , or by the kinetics of the heterogeneous reaction itself, which is expressed by the value of k_2^{ch} ; these relationships are presented in Eqs. 36–39:

$$k_{ox} = -k_2 A_p p_{O_2} y_c, \quad (36)$$

$$k_2 = \frac{k_2^{ch} \cdot k_2^{ph}}{k_2^{ch} + k_2^{ph}}, \quad (37)$$

$$k_2^{ch} = k_{0,2}^{ch} \cdot \exp(-E_{a2}^{ch} / RT), \quad (38)$$

$$k_2^{ph} = \frac{24 \cdot f_m \cdot D_0}{R \cdot d_p \cdot T_0^{1.75}} T^{0.75} \cdot 10^5. \quad (39)$$

Additionally, the values of the kinetic constants for the char oxidation are also obtained from the literature [34]-[35] depending on which coal or biomass is modelled.

From the char oxidation (Eq. 30), there is also a decrease in the oxygen mass and an increase in the carbon monoxide and carbon dioxide mass. These mass changes are sink/source terms to the continuous phase equations, and according to the stoichiometry in Eq. 30, these mass changes can be expressed as:

$$\dot{m}_{O_2} = \frac{1}{f_m} \left(\frac{M_{O_2}}{M_C} \right) \dot{m}_{C-} n_p, \quad (40)$$

$$\dot{m}_{CO} = - \left(2 - \frac{2}{f_m} \right) \left(\frac{M_{CO}}{M_C} \right) \dot{m}_{C-} n_p, \quad (41)$$

$$\dot{m}_{CO_2} = \left(1 - \frac{2}{f_m} \right) \left(\frac{M_{CO_2}}{M_C} \right) \dot{m}_{C-} n_p. \quad (42)$$

Finally, based on Eq. 29 and Eq. 35, the change in the overall particle mass expressed by Eq. 23 can be written in the following form:

$$\dot{m}_p = -\sum \dot{m}_k / n_p + \dot{m}_{C-} = \frac{m_p (1 - \frac{M_C |v_C|}{M_{coal/biomass}}) k_d + m_p k_{ox}}{(1 - \frac{m_C}{m_p} - \frac{m_{coal/biomass}}{m_p} (1 - \frac{M_C |v_C|}{M_{coal/biomass}}))}. \quad (43)$$

The local mass and enthalpy transfer processes between Lagrangian particles and their computational residence cell inside the gas phase time steps of the Navier-Stokes solver are resolved in more detail with a time-step sub-cycling method. For this purpose, simplified enthalpy and mass balances are solved for each particle and each cell during the time-step sub-cycling. These neglect some aspects, e.g., convective heat and mass transfer from neighbouring cells and local thermal radiation effects inside the cell. However, these are considered and updated again in the next solution step of the Eulerian gas phase solver after sources from the Lagrangian phase have been added. The particle radiation effects are considered globally using the P1 radiation model included in the gas phase solver. Enthalpy exchange during the devolatilisation and char oxidation (enthalpy transfer from reaction and convective enthalpy) is calculated separately for the particle and for the gas temperature in the residence cells of the particles.

For the conservation of enthalpy for a solid particle, the following equation can be written:

$$\dot{\mathcal{E}}_p = \frac{1}{m_p c_p} \left(\frac{-f \Delta H_R \dot{m}_c}{M_C} + \alpha A (T_g - T_p) \right). \quad (44)$$

Similar to the enthalpy balance for the particle, the enthalpy of the continuous phase is:

$$\dot{\mathcal{E}}_g = \frac{\left[\left(\frac{-(1-f) \Delta H_R \dot{m}_c}{M_C} - \alpha A (T_g - T_p) \right) n_p + \sum \dot{m}_i c_{pi} (T_p - T_g) \right]}{\sum m_i (c_{pi} + \frac{dc_{pi}}{dT} T)}. \quad (45)$$

From these equations, the rates of particle and gas temperature change are calculated. The mass and enthalpy balance equations given above are applied in each cell of the computational domains during the integration of the Lagrangian particle phase to update the gas and particle properties and are solved by time-step sub-cycling using DVODE solver [29]. Furthermore, from these equations, the source terms for the species mass and enthalpy are collected transferring the impact of the thermo-chemical reactions from the particles to the Eulerian solver.

2.4.3. Volatile combustion

For the homogeneous gas phase reactions of volatile oxidation, a detailed chemistry approach is used. The source terms in each species transport equation (Eq. 5) and in the continuous phase mass, momentum and energy conservation equation (Eqs. 1-2 and Eq. 4) are calculated according to the Arrhenius law, which means that the reaction rates of each homogeneous reaction depend on the species concentration and temperature. The modelled homogeneous

reactions include a four-step mechanism of methane combustion, combustion of tar, represented by the gaseous specie C_6H_6 , and carbon monoxide oxidation. Only the combustion of these gaseous species is considered, since they are the devolatilisation products (see Eqs. 10 and 11). However the volatiles combustion process is dealing with much more species and is also much more complicated. But, the species used are intended to give a first representation of the characteristic reaction types of CO-oxidation, alkane-oxidation and tar-oxidation, taking place during pyrolysis. More details concerning the treated homogeneous reactions and their reaction rates can be found in our previous study [27].

2.5. Plastic combustion model

The thermal decomposition of different polymers has been at the centre of studies for several years [39]. Plastic waste has been reported to consist mainly of four polymers: polyethylene (PE), polypropylene (PP), polystyrene (PS), and polyvinylchloride (PVC) [40]. In this study, for the plastic combustion model, a reaction scheme dealing with polymers structured as C_nH_{2n} , e.g., PE, and PP, has been designed. For the validation of the plastic combustion model, only polypropylene was used. The reason for this is that, to the knowledge of the authors, currently no experimental data for the validation other plastic combustion models exist [18]. Therefore, the current plastic combustion model is based on PP's combustion behaviour. However, future research activities may include validation of the presented plastic combustion model with other commercial polymers.

Experimental data have clearly indicated that polypropylene degrades in a single-stage process [41]. This is described with the following equation for the mass change of a PP particle:

$$\dot{m}_p = -k_0 e^{\frac{-E_a}{RT_p}} m_p. \quad (46)$$

The values of the polypropylene decomposition kinetic constants, e.g., the pre-exponential factor and the activation energy, are obtained from the literature [42]. Here, it is assumed that the PP particle decomposes directly to the gas phase as PP vapour without any intermediate liquid phase. Therefore, the source for the continuous phase equations from the particles is:

$$\dot{m}_{PPvapour} = -\dot{m}_p n_p. \quad (47)$$

The enthalpy conservation of a PP particle can be written as:

$$\dot{T}_p = \frac{1}{m_p c_p} \left(\Delta H_R \dot{m}_p + \alpha A (T_g - T_p) \right). \quad (48)$$

Similar to the enthalpy balance for the particle, the enthalpy of the continuous phase is:

$$\dot{T}_g = \frac{\left[-\alpha A (T_g - T_p) n_p + \dot{m}_{PP\text{vapour}} c_{PP\text{vapour}} (T_p - T_g) \right]}{\sum m_i \left(c_{pi} + \frac{dc_{pi}}{dT} T \right)}. \quad (49)$$

The PP vapour is combusted in the continuous phase according to the Westbrook and Dryer [43] global reaction mechanism:



2.6. SRF combustion model

In this study, due to the complex and inhomogeneous composition of SRF, the modelling approach from Agraniotis et al. [18] is used to describe the SRF combustion. SRF is modelled as a mixture of two different fractions: the biodegradable fraction and the plastic fraction. Each fraction undergoes a different combustion procedure. The biodegradable fraction uses the biomass combustion model, whereas the plastic fraction uses the polypropylene combustion model, both of which have been elaborated on previously. Following the same study [18], the plastic fraction accounts for 20% of SRF's mass.

The used Lagrangian frame of reference for solid particles, allows treating particles differently according to their type, meaning that different particles react differently. In gas phase the volatiles are combusted in parallel by solving coupled system of reaction equations depending on local temperature conditions and availability of reactants. Thus, the heterogeneous reactions respectively devolatilisation or combustion of polypropylene can be treated in an additive way particle by particle, while the subsequent gas phase reactions are fully coupled.

3. Single Particle Test and Results

To further elaborate the numerical method and for plausibility checks and quantitative checks and balances, the models for coal/biomass and polypropylene combustion presented above were tested on a single particle in a single mesh cube. Different initial conditions were used (e.g., temperature, particle diameter) to test the presented numerical model.

For the calculation of a single biomass particle, for which the results are shown in Fig. 1(a), the initial particle diameter was set to 100 μ m, the initial particle temperature was set to 50 °C, the initial particle moisture content was set to 15%, and the ambient temperature in the single mesh cube was set to 1400 °C. Fig. 1(a) shows the evolution of different biomass particle components. First, the moisture evaporated and its mass fraction decreased to zero. At

the same time, the biomass fraction increased. Afterwards the devolatilisation began, the dry biomass released the volatile matter, its mass fraction decreased, and, correspondingly, the mass fraction of char increased. Parallel to the devolatilisation, the char was oxidized, and therefore, the mass fraction of ash in the particle increased rapidly. When the devolatilisation was complete, the char mass fraction achieved its maximum value, after which, due to the char oxidation, the char mass fraction steadily decreased and the ash mass fraction increased.

In Fig. 1(b), the biomass particle with the same initial conditions as in Fig. 1(a) was analysed. Fig. 1(b) shows the influence of different ambient temperatures in the single mesh cube on the decrease in the biomass particle diameter. First, the biomass diameter decreased due to moisture evaporation; then, during devolatilisation and simultaneous char oxidation, the diameter was strongly reduced. Furthermore, a greater temperature caused faster shrinking of the biomass particle. The observed particle diameter shrinking behaviour, which was influenced by different ambient temperatures, is also valid for the behaviour of the particle mass loss. The biomass particle lost its mass in the same sequence and by the same behaviour.

In Fig. 1(c), biomasses of different sizes with an initial particle temperature of 50 °C, an initial particle moisture content of 15%, and an ambient temperature in the single mesh cube of 1000 °C were analysed. The particle was heated up until it completely combusted, after which it cooled down to the cell ambient temperature. As expected, smaller particles tend to heat up faster than the larger particles. During the boiling process, the particle temperature remained the same.

For calculations of a single polypropylene particle, for which the results are shown in Fig. 2, the initial particle temperature was set to 50 °C, and the ambient temperature in the single mesh cube was set to 1000 °C. Fig. 2(a) shows the polypropylene particle mass loss during the simulated time. As expected, smaller particles decomposed quicker than larger particles. The mass of the polypropylene was also observed to not change until the decomposition began.

Fig. 2(b) shows the increase in the particle temperature during the simulation time. Here, the polypropylene particle temperature was observed to steadily increase until the decomposition process began. Then, the temperature increase slowed down due to the mass exchange consuming the reaction enthalpy. At the end of the decomposition process, the temperature again began to increase more rapidly due to the decreasing particle size and mass until the moment at which all polypropylene was decomposed. These phenomena are more visible with a larger particle size.

Fig. 2(c) shows the relation between polypropylene particle mass and temperature. Larger particles began to decompose quicker than smaller particles. What can also be seen in this figure is that within certain temperature ranges, particles lose most of their mass. This is related to Eq. 46, which governs the mass change of the PP particle. As observed from this equation, the change in PP particle mass is in linear relation with its initial mass.

The results gained from the single particle tests for the biomass and polypropylene particles show that different particle sizes and ambient temperatures have an expected effect on the heat-up and decomposition history of the particles. Furthermore, the reaction kinetics of the biomass combustion are shown to yield reasonable trends.

4. Large-scale cement calciner simulations

To demonstrate the application of the validated solid fuel combustion models for the numerical analysis of the co-firing process, the complex three-dimensional geometry of an industrial cement calciner was simulated. In Fig. 3, the geometry of the simulated cement calciner together with the boundary conditions used and the position of the plane cut used for presenting the results are shown. The simulated calciner consisted of two vertical cylindrical parts and a cylinder part connecting them. The burner was positioned on the top of the first vertical cylinder together with two tangential limestone and two tertiary air inlets. To enhance the swirling effect and mixing of the raw material and the solid fuel in the first vertical cylinder, the tertiary air inlets were positioned diametrically opposite of each other. Good mixing of the fuel and the raw material is essential for an efficient calcination process. At the bottom of the second vertical cylinder, the hot gas stream from the rotary kiln entered. The hot exhaust gases from the rotary kiln were used to enhance the calcination process. A converging-diverging section at the bottom of the second vertical cylinder was used to increase the velocity of the incoming hot gas stream. The calciner was 24 m high, and the diameter of the first cylindrical was 5.5 m, and the diameter of the second cylindrical part was 4.5 m. The connecting cylinder was 4 m in diameter and is positioned at a 60° angle between the two vertical cylinders.

A transient simulation was performed with a time-step of $5 \cdot 10^{-4}$ s. The pressure velocity coupling of the momentum and continuity equations was obtained using the SIMPLE algorithm. The differencing scheme used for the continuity was central differencing; the MINMOD relaxed scheme was used for the momentum and enthalpy balances [29]; an Upwind scheme was used for the turbulence and scalar transport equations. Turbulence was

modelled using the standard $k-\varepsilon$ model. The P1 radiation model was used to model the radiative heat transfer and particle effects.

Because alternative fuels have different volatile and fixed carbon contents compared with coal, their flame shape differs somewhat from that of coal. Therefore, the combustion of alternative fuels as well as their co-firing with coal must be carefully evaluated to ensure effective operation. In this study, six different co-firing cases were simulated to investigate the influence of alternative fuels in practical operation on the flame shape and pollutant formation.

The boundary conditions used for the six simulation cases are given in Table 2. Furthermore, for consistency and better understanding of the amount of coal that was substituted, in Table 2, the boundary conditions used for the reference coal combustion simulation case are also given.

5. Result and discussion

An important quantity to characterize the co-firing process is the thermal share of the substituting fuel in the fuel mix. In the co-firing results that will be discussed, there was a different thermal share of SRF in each simulation case. In the simulation results shown in Figs. 4-11, each co-firing case is denoted with a different letter. The reference case, where only coal was burned, is denoted with the letter (*a*). The first co-firing case, where the thermal share of coal was 90 % and SRF was 10 %, is denoted with the letter (*b*). The second co-firing case, where the thermal share of coal was 70 % and SRF was 30 %, is denoted with the letter (*c*). In the third co-firing case, which is denoted with the letter (*d*), the thermal share of the coal and SRF was equal, which means that each fuel has a thermal share of 50 % in the fuel mix. The fourth co-firing case, where the thermal share of coal was 30 % and SRF was 70 %, is denoted with the letter (*e*). In the final co-firing case, denoted with the letter (*f*), only SRF was used as a fuel, which means that a full fuel substitution was analysed in this co-firing case.

In Fig. 4, the temperature field inside the calciner for the six calculated cases is shown. In this figure, from the left-hand side to the right-hand side, the temperature fields for the reference coal case and the five SRF co-firing cases are shown. The figure shows that in all simulated cases, the temperature throughout the calciner is more or less uniform and approximately 1300 K except in the near-burner region. This is due to the strong endothermic calcination reaction where limestone particles using the available enthalpy in the gas phase thermally decompose. Furthermore, there are some differences in the temperature field in the

near-burner region. In case (a), which is the case where only coal is used as a fuel, the temperature is the greatest. When compared to the other cases, it can be observed that, from the left-hand side to the right-hand side, as the thermal share of SRF in the fuel mix is increased, the temperature profile in the near-burner region changes. A decrease in the middle of the temperature peak can be observed. This is due to the greater moisture content in the biomass fraction of the SRF than that of coal, which means that heat is used for drying the SRF particles. These particles need more time to dry, begin to devolatilise, and char to oxidize.

The observation from Fig. 4 is also related to the results shown in Fig. 5. Fig. 5 shows the velocity field inside the calciner for the six calculated cases. In this figure, from the left-hand side to the right-hand side, the velocity fields for the reference coal case and the five SRF co-firing cases are shown. The figure shows that in all cases, the greatest velocity is at the bottom of the calciner where the high velocity stream of exhaust gases coming from the rotary kiln enters. What can also be seen from this figure is that an increase in the thermal share of SRF in the fuel mix does not significantly influence the velocity field. This means that SRF particles of greater moisture content that are carried by the gas stream through the cement calciner require more time to dry and to begin to combust.

In Fig. 6, the CH_4 mole fraction inside the calciner for the six calculated cases is shown. In this figure, from the left-hand side to the right-hand side, the CH_4 mole concentrations for the reference coal case and the five SRF co-firing cases are shown. The figure shows the difference in the CH_4 concentrations for all calculated cases. These differences are due to the difference in fuel properties of the coal and SRF. Coals tend to have a greater fixed carbon content and less volatile matter, whereas biomasses tend to have a lower fixed carbon content and more volatile matter. Therefore, from Fig. 5, it is clear that the CH_4 concentration in the near-burner region increased as the SRF thermal share in the fuel mix increased.

Fig. 7 shows the CO_2 mole fraction inside the calciner for the six calculated cases. In this figure, from the left-hand side to the right-hand side, the CO_2 mole concentrations for the reference coal case and the five SRF co-firing cases are shown. The figure clearly shows the differences in the CO_2 concentrations for all calculated cases. The reason for these differences is the endothermic calcination reaction, which is predominantly a temperature-driven process. Fig. 4 shows that a temperature decrease was observed as the SRF thermal share increased; therefore, the calcination reaction also follows this trend. As the SRF thermal share is increased, the calcination process is slower and less CO_2 from this reaction is emitted.

In Fig. 8, the CO mole fraction inside the calciner for the six calculated cases is shown. In this figure, from the left-hand side to the right-hand side, the CO mole concentrations for the

reference coal case and the five SRF co-firing cases are shown. From this figure, it can be observed that the CO concentrations decreased as the SRF thermal share increased. This is again a result of the difference in fuel properties of coal and SRF. Coal has a greater fixed carbon content, and biomasses tend to have a lower fixed carbon content. The fixed carbon, which remains in the particles after the devolatilisation, oxidizes and, depending on the particle temperature and size, forms CO and CO₂. Correspondingly, there is more CO in the near-burner region where the combustion process is taking place.

Fig. 9 shows the H₂O mole fraction inside the calciner for the six calculated cases. In this figure, from the left-hand side to the right-hand side, the H₂O mole concentrations for the reference coal case and the five SRF co-firing cases are shown. The concentration of H₂O increased from the left-hand side to the right-hand side of the figure. This means that the H₂O concentrations increased as the SRF thermal share increased. The reason for this is the greater moisture content in the biomass fraction of the SRF than that of coal. These greater H₂O concentrations are related to the evaporation of moisture from the SRF, which means that heat is used to dry SRF particles.

In Fig. 10, the mass fraction of lime in the raw material particle inside the calciner for the six calculated cases is shown. In this figure, from the left-hand side to the right-hand side, the lime mass fractions in the raw material particle for the reference coal case and the five SRF co-firing cases are shown. In this figure, red particles represent raw material particles that fully decomposed to lime. Blue particles represent particles that had not decomposed. Fresh raw material decomposes to lime more quickly in the case where only coal is burned. However, in all six cases, only fully decomposed raw material particles, e.g., lime particles, exit the cement calciner. The reason for this is that in all six cases, a sufficient amount of heat was provided for the calcination reaction to occur.

Fig. 11 shows the mass fraction of char in the fuel particle inside the calciner for the six calculated cases. In this figure, from the left-hand side to the right-hand side, the char mass fractions in the raw material particle for the reference coal case and the five SRF co-firing cases are shown. In this figure, red particles represent fuel particles that have the greatest mass fraction of char in the fuel particle. Blue particles represent particles that have the least mass fraction of char in the fuel particle. It can be observed that from the left-hand side to the right-hand side of the figure, the amount of unburned char particles that are exiting the calciner is increased. The case with the lowest amount of unburned char that is exiting the calciner is the case where only coal is burned. However, the case with the greatest amount of unburned char that is exiting the calciner is the case where only SRF is burned. This result is

due to the temperature distribution inside of the cement calciner and the greater moisture content in SRF than in coal. The SRF particles need more time to dry, to begin to devolatilise, and for the char to oxidize. Here, there should be further elaboration on why there is a difference in the particle colouring between the first five cases and the case where only SRF is burned. The reason for this lies in the difference in fuel properties of the coal and SRF. Coal has a greater fixed carbon content, whereas the biomass fraction of SRF has a lower fixed carbon content. In the case where only SRF is burned, there are no coal particles of greater fixed carbon content.

To ensure the adequate conditions for a complete calcination reaction inside cement calciners, a good understanding of the different co-firing concepts is essential. The use of experimental methods for this purpose is complex and expensive. Therefore, the use of numerical techniques is an attractive way to obtain the necessary information and can, at a minimum, supplement the experimental analysis. Furthermore, the results gained by the numerical simulations provide detailed information about the flow characteristics and thermo-chemical reactions that occur inside a cement calciner. The results obtained from this study show some interesting features of the flow and pollutant formation, which can aid in understanding the different co-firing conditions for the calculated cement calciner. Although the comparison of numerically obtained results with experimental data is essential, experimental measurements were not available for this calciner. Even though there are no experimental measurements for this calciner, the predictions shown are based on separately validated sub-models. Therefore, these results are expected to correctly indicate the trends caused by various SRF thermal shares.

6. Conclusion

Due to different fuel properties than that of coal, alternative fuels have a direct impact on the performance of existing pulverized coal fired furnaces. Consequently, the combustion behaviour of these fuels and especially the co-firing of such fuels with coal must be carefully analysed in the existing furnaces to have stable operating conditions. Computer modelling of alternative fuel combustion and co-firing with coal provides a valuable tool that can be used for the investigation and better understanding of particle kinetics and pollutant emissions from cement combustion systems.

The main objectives of this study were the following:

- present the modelling approach for the combustion of pulverized coal, biomass, plastic, and solid recovered fuel;

- present the plausibility checks and quantitative checks and balances of the presented combustion models in the form of tests of a single particle in a single mesh cube;
- demonstrate the large-scale application of the presented models; and
- evaluate six different pulverized coal and solid recovered fuel co-firing modes inside a cement calciner.

The numerical models for the pulverized solid fuel combustion were implemented into a commercial CFD code AVL FIRE[®] taking into account the major effects that influence these processes. The numerical models were described in detail to accurately explain the thermo-chemical processes that govern the combustion process.

Validated models were used to simulate the complex three-dimensional geometry of a large-scale cement calciner. The thermal share of the solid recovered fuel in these six simulations varied from 0 % to 100 %. The results obtained, which include temperature, velocity, species concentrations, and char and lime mass fractions in the particles, provide useful conclusions regarding the maximal allowed coal substitution rate for stable cement calciner operation. Furthermore, the obtained results show that pre-drying of an alternative fuel is essential for efficient calciner operation to use the provided heat for the calcination process and not to dry the SRF particles. The results obtained from these simulations can be used to better understand the thermo-chemical reaction occurring inside the calculated calciners and to make improvements.

By using the presented combustion models for the evaluation of different co-firing modes, time-consuming and costly experimental studies can be avoided. Therefore, numerical simulations are a useful tool that can be used to study and improve different co-firing concepts in existing pulverized fuel combustion units. Furthermore, it should also be mentioned that the presented models can be used to investigate practical engineering options. Some such practical engineering aspects include the investigation of the following:

- the temperature hot spots in the near-wall regions with the goal of reducing the thermal load on the wall;
- the particle mixing phenomena with the goal of increasing the reaction rate of limestone thermal degradation;
- the length of different units with the goal of ensuring complete limestone decomposition and fuel oxidation;
- the complete combustion versus complete calcination with the goal of reducing fuel consumption;

- the danger of erosion in high velocity regions close to the wall with the goal of minimizing the wall erosion effects;
- the influence of different thermal shares of different alternative fuels with the goal of creating a stable manufacturing process;
- the influence of various process air streams with the goal of minimizing the thermal losses; and
- the concentration of CO₂, CO and other pollutants with the goal of reducing the environmental impact of the manufacturing process.

Acknowledgements

The authors wish to thank Dr. P. Priesching and Dr. R. Tatschl from the CFD Development group at AVL-AST, Graz, Austria, for their continuous support and useful discussions during the development of the numerical models used in this study.

Nomenclature

A_p	particle surface, m ²
$\overline{c_p}$	specific heat capacity of coal or biomass, ash and char mixture, J kg ⁻¹ K ⁻¹
c_{pi}	specific heat capacity of gas component, J kg ⁻¹ K ⁻¹
$c_{PPVvapour}$	specific heat capacity of polypropylene vapour, J kg ⁻¹ K ⁻¹
C_p	water vapour concentration at the particle surface, kg mol m ⁻³
C_g	concentration of water vapour in the gas, kg mol m ⁻³
d_p	particle diameter, m
D_0	oxygen diffusion coefficient, dimensionless
D_w	diffusion coefficient of water vapour in the gas, m ² s ⁻²
E	internal energy, J kg ⁻¹
E_a	activation energy for polypropylene decomposition, J mol ⁻¹
E_{a1}	activation energy for devolatilisation, J mol ⁻¹
E_{a2}	activation energy for char oxidation, J mol ⁻¹
f	reaction enthalpy factor, dimensionless
f_m	mechanism factor, dimensionless

f_{CO}	carbon monoxide factor, dimensionless
F_{idr}	drag force vector, N
F_{ig}	force including effects of gravity and buoyancy vector, N
g	gaseous, dimensionless
g_i	gravitational acceleration vector, $m\ s^{-2}$
h_{latent}	latent heat, $J\ kg^{-1}$
ΔH_R	reaction enthalpy, $J\ mol^{-1}$
k_0	pre-exponential factor for polypropylene decomposition, s^{-1}
$k_{0,1}$	devolatilisation pre-exponential factor, s^{-1}
$k_{0,2}^{ch}$	char oxidation pre-exponential factor, s^{-1}
k_1	devolatilisation reaction rate, s^{-1}
k_2	char oxidation reaction rate, s^{-1}
k_2^{ch}	char oxidation chemical reaction rate, $kg\ m^{-2}\ s^{-1}\ Pa^{-1}$
k_d	overall devolatilisation reaction rate, s^{-1}
k_2^{ph}	char oxidation physical reaction rate, $kg\ m^{-2}\ s^{-1}\ Pa^{-1}$
k_{ox}	overall char oxidation reaction rate, s^{-1}
k_w	mass transfer coefficient, $m\ s^{-1}$
m_{ash}	ash mass, kg
m_C	char mass, kg
$m_{coal/biomass}$	coal or biomass mass, kg
m_i	i -th gas component mass, kg
m_p	particle mass, kg
\dot{m}_{ash}	mass transfer of ash, $kg\ s^{-1}$
\dot{m}_{C+}	increase in char mass due to devolatilisation, $kg\ s^{-1}$
\dot{m}_{C-}	decrease in char mass due to char oxidation, $kg\ s^{-1}$
$\dot{m}_{coal/biomass}$	coal or biomass mass change, $kg\ s^{-1}$
\dot{m}_{CO}	mass transfer of carbon monoxide, $kg\ s^{-1}$
\dot{m}_{CO_2}	mass transfer of carbon dioxide, $kg\ s^{-1}$

\dot{m}_i	mass transfer of i-th gas component, kg s ⁻¹
\dot{m}_{O_2}	mass transfer of oxygen, kg s ⁻¹
\dot{m}_p	mass transfer of a particle, kg s ⁻¹
$\dot{m}_{PPvapour}$	mass transfer of polypropylene vapour, kg s ⁻¹
\dot{m}_{Y_k}	mass transfer of k-th gas component due to devolatilisation, kg s ⁻¹
M_C	char molecular weight, g mol ⁻¹
$M_{coal/biomass}$	coal or biomass molecular weight, g mol ⁻¹
M_{CO}	carbon monoxide molecular weight, g mol ⁻¹
M_{CO_2}	carbon dioxide molecular weight, g mol ⁻¹
M_{H_2O}	water vapour molecular weight, g mol ⁻¹
M_{O_2}	oxygen molecular weight, g mol ⁻¹
M_{Y_k}	k-th gas component molecular weight, g mol ⁻¹
n_p	number of particles per parcel, dimensionless
p	total pressure, Pa
p_{O_2}	oxygen partial pressure, Pa
p_{sat}	saturation pressure, Pa
R	universal gas constant, J mol ⁻¹ K ⁻¹
Re_p	particle Reynolds number, dimensionless
s	solid, dimensionless
S_C	mass source, kg s ⁻¹
S_E	energy source, W m ⁻³
S_M	momentum source, N m ⁻³
S_{Y_k}	k-th gas component source, kg s ⁻¹
Sc	Schmidt number, dimensionless
Sh	Sherwood number, dimensionless
T	temperature, K
T_0	reference temperature, K
T_g	gas temperature, K

T_p	particle temperature, K
\dot{T}_p	change in particle temperature, K s ⁻¹
t	time, s
u_{ip}	particle velocity vector, m s ⁻¹
v_i, v_j	velocity vector, m s ⁻¹
X_{H_2O}	water vapour molar fraction, dimensionless
y_C	mass fraction of char remaining in the particle, dimensionless
$y_{coal/biomass}$	mass fraction of coal or biomass remaining in the particle, dimensionless
Y_k	k -th gas component mass fraction, dimensionless

Greek letters

α	convective heat transfer coefficient, W m ⁻² K ⁻¹
Γ	diffusion coefficient, dimensionless
δ_{ij}	Cronecker symbol, dimensionless; for $i=j$ $\delta_{ij} = 1$
ε	emissivity, dimensionless
λ	thermal conductivity, W m ⁻¹ K ⁻¹
μ	dynamic viscosity, Pa s
ν_C	char stoichiometry number from devolatilisation, dimensionless
ν_{Y_k}	k -th gas component stoichiometry number from devolatilisation, dimensionless
ρ	density, kg m ⁻³
σ	Stefan-Boltzmann's constant, W m ⁻² K ⁻⁴
τ_{ij}	stress tensor, Pa

References

- [1] Yong JY, Klemeš JJ, Varbanov PS, Huisingh D. Cleaner Energy for Cleaner Production: Modelling, Simulation, Optimisation and Waste Management. J Clean Prod 2015. doi:10.1016/j.jclepro.2015.10.062.
- [2] Hu Y, Li H, Yan J. Numerical investigation of heat transfer characteristics in utility

- boilers of oxy-coal combustion. *Appl Energy* 2014;130:543–51. doi:10.1016/j.apenergy.2014.03.038.
- [3] Mikulčić H, Vujanović M, Duić N. Reducing the CO₂ emissions in Croatian cement industry. *Appl Energy* 2013;101:41–8. doi:10.1016/j.apenergy.2012.02.083.
- [4] Li J, Paul MC, Younger PL, Watson I, Hossain M, Welch S. Characterization of biomass combustion at high temperatures based on an upgraded single particle model. *Appl Energy* 2015;156:749–55. doi:10.1016/j.apenergy.2015.04.027.
- [5] Ng WPQ, Lam HL, Varbanov PS, Klemeš JJ. Waste-to-Energy (WTE) network synthesis for Municipal Solid Waste (MSW). *Energy Convers Manag* 2014;85:866–74. doi:10.1016/j.enconman.2014.01.004.
- [6] Al-Salem SM, Lettieri P, Baeyens J. Recycling and recovery routes of plastic solid waste (PSW): A review. *Waste Manag* 2009;29:2625–43. doi:10.1016/j.wasman.2009.06.004.
- [7] Pinto F, André RN, Carolino C, Miranda M, Abelha P, Direito D, et al. Gasification improvement of a poor quality solid recovered fuel (SRF). Effect of using natural minerals and biomass wastes blends. *Fuel* 2014;117:1034–44. doi:10.1016/j.fuel.2013.10.015.
- [8] Rada EC, Andreottola G. RDF/SRF: Which perspective for its future in the EU. *Waste Manag* 2012;32:1059–60. doi:10.1016/j.wasman.2012.02.017.
- [9] Zhou C, Zhang Q, Arnold L, Yang W, Blasiak W. A study of the pyrolysis behaviors of pelletized recovered municipal solid waste fuels. *Appl Energy* 2013;107:173–82. doi:10.1016/j.apenergy.2013.02.029.
- [10] Lu J-J, Chen W-H. Investigation on the ignition and burnout temperatures of bamboo and sugarcane bagasse by thermogravimetric analysis. *Appl Energy* 2015;160:49–57. doi:10.1016/j.apenergy.2015.09.026.
- [11] Borello D, Venturini P, Rispoli F, Rafael SGZ. Prediction of multiphase combustion and ash deposition within a biomass furnace. *Appl Energy* 2013;101:413–22. doi:10.1016/j.apenergy.2012.04.031.
- [12] Liu X, Bansal RC. Integrating multi-objective optimization with computational fluid dynamics to optimize boiler combustion process of a coal fired power plant. *Appl Energy* 2014;130:658–69. doi:10.1016/j.apenergy.2014.02.069.

- [13] Bhuiyan A a., Naser J. Computational modelling of co-firing of biomass with coal under oxy-fuel condition in a small scale furnace. *Fuel* 2015;143:455–66. doi:10.1016/j.fuel.2014.11.089.
- [14] Dong C, Yang Y, Yang R, Zhang J. Numerical modeling of the gasification based biomass co-firing in a 600 MW pulverized coal boiler. *Appl Energy* 2010;87:2834–8. doi:10.1016/j.apenergy.2009.05.033.
- [15] Holtmeyer ML, Kumfer BM, Axelbaum RL. Effects of biomass particle size during cofiring under air-fired and oxyfuel conditions. *Appl Energy* 2012;93:606–13. doi:10.1016/j.apenergy.2011.11.042.
- [16] Gubba SR, Ingham DB, Larsen KJ, Ma L, Pourkashanian M, Tan HZ, et al. Numerical modelling of the co-firing of pulverised coal and straw in a 300 MWe tangentially fired boiler. *Fuel Process Technol* 2012;104:181–8. doi:10.1016/j.fuproc.2012.05.011.
- [17] Karampinis E, Nikolopoulos N, Nikolopoulos a., Grammelis P, Kakaras E. Numerical investigation Greek lignite/cardoon co-firing in a tangentially fired furnace. *Appl Energy* 2012;97:514–24. doi:10.1016/j.apenergy.2011.12.032.
- [18] Agraniotis M, Nikolopoulos N, Nikolopoulos A, Grammelis P, Kakaras E. Numerical investigation of Solid Recovered Fuels' co-firing with brown coal in large scale boilers - Evaluation of different co-combustion modes. *Fuel* 2010;89:3693–709. doi:10.1016/j.fuel.2010.07.030.
- [19] Ariyaratne WKH, Malagalage A, Melaaen MC, Tokheim L-A. CFD modelling of meat and bone meal combustion in a cement rotary kiln – Investigation of fuel particle size and fuel feeding position impacts. *Chem Eng Sci* 2015;123:596–608. doi:10.1016/j.ces.2014.10.048.
- [20] Mikulčić H, von Berg E, Vujanović M, Duić N. Numerical study of co-firing pulverized coal and biomass inside a cement calciner. *Waste Manag Res* 2014;32:661–9. doi:10.1177/0734242X14538309.
- [21] Mikulčić H. Numerical modelling of thermo- chemical processes inside a cement calciner for a cleaner cement production. PhD Thesis, Zagreb 2015.
- [22] Yin C. On gas and particle radiation in pulverized fuel combustion furnaces. *Appl Energy* 2015;157:554–61. doi:10.1016/j.apenergy.2015.01.142.
- [23] Li J, Brzdekiewicz A, Yang W, Blasiak W. Co-firing based on biomass torrefaction in

- a pulverized coal boiler with aim of 100% fuel switching. *Appl Energy* 2012;99:344–54. doi:10.1016/j.apenergy.2012.05.046.
- [24] Johansen JM, Gadsbøll R, Thomsen J, Jensen PA, Glarborg P, Ek P, et al. Devolatilization kinetics of woody biomass at short residence times and high heating rates and peak temperatures. *Appl Energy* 2016;162:245–56. doi:10.1016/j.apenergy.2015.09.091.
- [25] Ström H, Thunman H. A computationally efficient particle submodel for CFD-simulations of fixed-bed conversion. *Appl Energy* 2013;112:808–17. doi:10.1016/j.apenergy.2012.12.057.
- [26] Mikulčić H, Vujanović M, Duić N. Improving the sustainability of cement production by using numerical simulation of limestone thermal degradation and pulverized coal combustion in a cement calciner. *J Clean Prod* 2015;88:262–71. doi:10.1016/j.jclepro.2014.04.011.
- [27] Mikulčić H, von Berg E, Vujanović M, Priesching P, Tatschl R, Duić N. Numerical analysis of cement calciner fuel efficiency and pollutant emissions. *Clean Technol Environ Policy* 2013;15:489–99. doi:10.1007/s10098-013-0607-5.
- [28] Mikulčić H, von Berg E, Vujanović M, Priesching P, Perković L, Tatschl R, et al. Numerical modelling of calcination reaction mechanism for cement production. *Chem Eng Sci* 2012;69:607–15. doi:10.1016/j.ces.2011.11.024.
- [29] AVL FIRE® VERSION 2014 2014.
- [30] Mikulčić H, Vujanović M, Ashhab MS, Duić N. Large eddy simulation of a two-phase reacting swirl flow inside a cement cyclone. *Energy* 2014;75:89–96. doi:10.1016/j.energy.2014.04.064.
- [31] Yin C, Yan J. Oxy-fuel combustion of pulverized fuels: Combustion fundamentals and modeling. *Appl Energy* 2016;162:742–62. doi:10.1016/j.apenergy.2015.10.149.
- [32] Williams a., Jones JM, Ma L, Pourkashanian M. Pollutants from the combustion of solid biomass fuels. *Prog Energy Combust Sci* 2012;38:113–37. doi:10.1016/j.peccs.2011.10.001.
- [33] Elfasakhany A, Tao L, Espenas B, Larfeldt J, Bai XS. Pulverised wood combustion in a vertical furnace: Experimental and computational analyses. *Appl Energy* 2013;112:454–64. doi:10.1016/j.apenergy.2013.04.051.

- [34] Wang G, Zander R, Costa M. Oxy-fuel combustion characteristics of pulverized-coal in a drop tube furnace. *Fuel* 2014;115:452–60. doi:10.1016/j.fuel.2013.07.063.
- [35] Wang G, Silva RB, Azevedo JLT, Martins-Dias S, Costa M. Evaluation of the combustion behaviour and ash characteristics of biomass waste derived fuels, pine and coal in a drop tube furnace. *Fuel* 2014;117:809–24. doi:10.1016/j.fuel.2013.09.080.
- [36] Ma L, Jones JM, Pourkashanian M, Williams a. Modelling the combustion of pulverized biomass in an industrial combustion test furnace. *Fuel* 2007;86:1959–65. doi:10.1016/j.fuel.2006.12.019.
- [37] Ranz WE, Marshall WR. Evaporation from drops - Part 1. *Chem Eng Prog* 1952;48:141–8.
- [38] Goerner K. *Technical combustion systems: fundamentals, modelling, simulation* 1991.
- [39] Peterson JD, Vyazovkin S, Wight CA. Kinetics of the Thermal and Thermo-Oxidative Degradation of Polystyrene , Polyethylene and Poly (propylene) 2001:775–84.
- [40] Al-Salem SM, Lettieri P, Baeyens J. The valorization of plastic solid waste (PSW) by primary to quaternary routes: From re-use to energy and chemicals. *Prog Energy Combust Sci* 2010;36:103–29. doi:10.1016/j.pecs.2009.09.001.
- [41] Gersten J, Fainberg V, Hetsroni G, Shindler Y. Kinetic study of the thermal decomposition of polypropylene , oil shale , and their mixture 2000;79:2–8.
- [42] Westerhout RWJ, Waanders J, Kuipers JAM, Swaaij WPM Van. Kinetics of the Low-Temperature Pyrolysis of Polyethene , Polypropene , and Polystyrene Modeling , Experimental Determination , and Comparison with Literature Models and Data 1997:1955–64.
- [43] Westbrook CK, Livermore L, Ca L. Simplified Reaction Mechanisms for the Oxidation of Hydrocarbon Fuels in Flames 1981;27:31–43.

Figures captions

Fig. 1. Biomass single particle tests: (a) evolution of biomass components; (b) particle diameter in relation to the different ambient temperatures; (c) temperature increase for particles of different sizes.

Fig. 2. Polypropylene single particle tests: (a) particle mass loss over time; (b) particle temperature over time; (c) mass loss in relation to the temperature increase.

Fig. 3. Cement calciner geometry and boundary conditions.

Fig. 4. Temperature fields inside the calciner for the six calculated cases: (a) 100 % coal case; (b) 10 % SRF co-firing case; (c) 30 % SRF co-firing case; (d) 50 % SRF co-firing case; (e) 70 % SRF co-firing case; (f) 100 % SRF co-firing case.

Fig. 5. Velocity fields inside the calciner for the six calculated cases: (a) 100 % coal case; (b) 10 % SRF co-firing case; (c) 30 % SRF co-firing case; (d) 50 % SRF co-firing case; (e) 70 % SRF co-firing case; (f) 100 % SRF co-firing case.

Fig. 6. CH₄ mole fraction inside the calciner for the six calculated cases: (a) 100 % coal case; (b) 10 % SRF co-firing case; (c) 30 % SRF co-firing case; (d) 50 % SRF co-firing case; (e) 70 % SRF co-firing case; (f) 100 % SRF co-firing case.

Fig. 7. CO₂ mole fraction inside the calciner for the six calculated cases: (a) 100 % coal case; (b) 10 % SRF co-firing case; (c) 30 % SRF co-firing case; (d) 50 % SRF co-firing case; (e) 70 % SRF co-firing case; (f) 100 % SRF co-firing case.

Fig. 8. CO mole fraction inside the calciner for the six calculated cases: (a) 100 % coal case; (b) 10 % SRF co-firing case; (c) 30 % SRF co-firing case; (d) 50 % SRF co-firing case; (e) 70 % SRF co-firing case; (f) 100 % SRF co-firing case.

Fig. 9. H₂O mole fraction inside the calciner for the six calculated cases: (a) 100 % coal case; (b) 10 % SRF co-firing case; (c) 30 % SRF co-firing case; (d) 50 % SRF co-firing case; (e) 70 % SRF co-firing case; (f) 100 % SRF co-firing case.

Fig. 10. Mass fraction of lime in the raw material particle inside the calciner for the six calculated cases: (a) 100 % coal case; (b) 10 % SRF co-firing case; (c) 30 % SRF co-firing case; (d) 50 % SRF co-firing case; (e) 70 % SRF co-firing case; (f) 100 % SRF co-firing case.

Fig. 11. Mass fraction of char in the fuel particle inside the calciner for the six calculated cases: (a) 100 % coal case; (b) 10 % SRF co-firing case; (c) 30 % SRF co-firing case; (d) 50 % SRF co-firing case; (e) 70 % SRF co-firing case; (f) 100 % SRF co-firing case.

Table 1

An overview of the modelling approach in previous studies.

Model	Description	Reference
Particle tracking	Tracking of the solid particles through the gas phase	[26]
Multi-phase flow	Coupling of the gas and solid phase	[27]
Calcination process	Detailed description of limestone thermal decomposition and validation of the model	[28]
Coal combustion	Detailed description of the coal combustion model	[26]
Biomass combustion	Detailed description of the biomass combustion model	[20]
SRF combustion	Detailed description of the SRF combustion model	[21]
Model validations	Comparison between experimental data and the numerical predictions for each solid fuel combustion model	[21]

Table 2

Boundary conditions for the large-scale calciner simulation.

	Case (a)	Case (b)	Case (c)	Case (d)	Case (d)	Case (d)
	T [°C]			Mass flow rate [kg h ⁻¹]		
Limestone 1+2	720			147,900		
Tertiary air 1	950			49,600		
Tertiary air 2	950			49,600		
Primary air	80			16,200		
Secondary air	950			33,065		
Coal	60	14,811	13,330	10,368	7,406	4,443
SRF Biomass fraction	60	-	1,793	5,379	8,965	12,550
SRF Plastic fraction	60	-	176	527	878	1,230
Hot gas from rotary kiln	1,100			110,600		
Outlet (Static Pressure)				10 ⁵ Pa		